Composite Structures 304 (2023) 116393

Contents lists available at ScienceDirect

Composite Structures

journal homepage: www.elsevier.com/locate/compstruct

Analysis and validation of a scaled, launch-vehicle-like composite cylinder under axial compression

Michelle Tillotson Rudd [a], David J. Eberlein [b], W. Allen Waters [c], Nathaniel W. Gardner [d], Marc R. Schultz [d], Chiara Bisagni [b,*]

[a] NASA Marshall Space Flight Center, Huntsville, AL 35812, USA
[b] Delft University of Technology, Faculty of Aerospace Engineering, Delft 2629HS, Netherlands
[c] Analytical Mechanics Associates, Hampton, VA 23666, USA
[d] NASA Langley Research Center, Hampton, VA 23681, USA

ARTICLE INFO

Keywords:
Composite cylindrical shell
Unconventional layup
Test
Buckling propagation
Measured imperfection

ABSTRACT

Launch vehicle structures, such as payload adapters and interstages, are increasingly designed and constructed using composite materials due to their high stiffness- and strength-to-weight ratios. Therefore, it is important to develop a validated finite element modeling methodology for designing and analyzing composite launch-vehicle shell structures. This can be achieved, in part, by correlating high-fidelity numerical models with test data. Buckling is often an important failure mode for cylindrical shells, and the buckling response of such structures is also often quite sensitive to imperfections in geometry and loading. Hence, it is crucial to understand the model parameters and details required to accurately predict the buckling load and behavior of composite cylindrical shells, especially if the shell is buckling critical. The inclusion of as-built features, such as radial imperfections, thickness variations, and loading imperfections can help improve the correlation between test and analysis. To demonstrate such an approach, a validated modeling methodology that was used to predict the buckling behavior of a scaled component for a launch-vehicle-like structure is presented, and results from the model are compared with experimental results. The modeling approach presented herein was used to successfully predict the buckling behavior.

1. Introduction

Launch-vehicle designs regularly incorporate thin-walled cylindrical shell structures. The use of composite materials to construct these structures, like payload adapters and interstages, has become more common in recent years. When axially compressed, thin-walled shells are highly susceptible to global buckling, which results in a sudden loss in load-carrying capability under axial compression. It is well known that the buckling behavior is highly dependent on sources of variations from theoretically ideal shells. These variations may include, but are not limited to, radial geometric imperfections, thickness variations, and loading nonuniformity. Thus, these variations can make it difficult to predict the buckling load, even with state-of-the-art analysis tools. Therefore, it is important to have an experimentally validated modeling methodology to provide confidence in the predicted buckling behavior of a composite cylinder. A validated finite element methodology can be used to assess the sensitivity of the shell to imperfections and may also be used to assess new design approaches for buckling-critical launch vehicle structures.

Prior to advances in computer simulations, researchers depended on analytical methods to predict the buckling loads of composite cylinders. Koiter [1] noted that the inclusion of radial imperfections was important when predicting the buckling load of a composite cylinder. To predict the buckling load prior to test, researchers such as Bert, et al. [2], Card [3], Tennyson and Muggeridge [4], and Herakovich [5] measured the amplitude of the radial geometric imperfection of test articles. An assumed shape of this amplitude was then incorporated into the analytical solution as a prebuckling deformation in order to best predict the buckling load.

Unlike analytical methods, a greater level of detail can easily be included in finite element models (FEMs) to more closely represent as-manufactured physical composite structures. Hilburger and Starnes [6] used the general-purpose finite element code STAGS (Structural Analysis of General Shells) to predict the buckling performance of four

* Corresponding author.
E-mail address: C.Bisagni@tudelft.nl (C. Bisagni).

https://doi.org/10.1016/j.compstruct.2022.116393
Received 20 May 2022; Received in revised form 20 September 2022; Accepted 18 October 2022
Available online 23 October 2022

composite cylinders. Validation tests, or tests conducted to validate the FEM, enabled the authors to investigate significant details, such as radial geometric imperfections, ply gaps, thickness imperfections, shell-end geometric imperfections, nonuniform loading, and elastic boundary conditions. Khakimova, et al. [7] included fiber volume fraction into their finite element model in addition to radial imperfections and thickness variations. They also showed the predicted buckling load converged to the tested buckling load by increasing the level of as-built details into their models.

Incorporating the as-built details of a composite cylinder into the FEM is important, but it is also necessary to understand how analysis parameters such as element type, mesh size, and the analysis solver influence the predicted buckling behavior. To address this uncertainty, Bisagni [8] conducted an extensive numerical study using the general-purpose finite element code, Abaqus. This study was completed before testing a carbon fiber reinforced polymer (CFRP) cylinder with a layup of [0/45/−45/0]. In this investigation, Bisagni performed linear eigenvalue, nonlinear Riks, and dynamic buckling analyses. The author noted there were negligible differences between the Riks and dynamic solutions with respect to the nonlinear behavior. In addition, a mesh convergence study was performed using the four-node shell element with reduced integration (S4R). The outcomes of this assessment led the author to use the S4R element with a mesh size of 0.6 elements/degree around the circumference and to use the dynamic solver. Priyadarsini, et al. [9] completed a similar study to determine the same element type, mesh density, and solver to assess the buckling behavior of four identical CFRP laminate specimens with a layup of $[0/45/-45/0]_S$. Ghalghachi, et al. [10] completed five buckling tests with five glass fabric reinforced polymer cylindrical shells. Ghalghachi, et al. used the same program and S4R element as Bisagni and Priyadarsini, et al., but used the Riks method to investigate the buckling behavior. The aforementioned authors studied constant stiffness cylinders, while other researchers have developed FEMs with similar model parameters to investigate the buckling behavior of variable stiffness composite cylinders and composite cylinders with cutouts [11–15].

Finite element models validated by testing have provided researchers with enhanced confidence in their numerical tools to develop probabilistic-based-design approaches for buckling-critical composite cylinders. Degenhardt, et al. [16] used a validated high-fidelity model to perform a Monte Carlo simulation that addressed the sensitivities to imperfections. From that, they determined the buckling knockdown factor — used in design to account for differences between test and analysis — for a composite cylinder with a radius/thickness ratio of 500 could be increased from the recommended knockdown factor calculated using NASA-SP-8007 [17]. Schillo, et al. [18] tested eleven nominally identical layups and developed a validated model to identify the influence of uncertainties for a reliability-based design approach.

In addition to probabilistic approaches, other researchers have identified the benefits of using validated models to develop new buckling knockdown factors. After validating a finite element model with testing, Hühne, et al. [19] proposed a less conservative lower bound buckling knockdown factor methodology using the single perturbation load approach (SPLA). These factors have the potential to be less conservative than those recommended for the empirical design approach in NASA-SP-8007, which may lead to mass savings of thin-walled shell structures made from composites. Similar to the SPLA, Wagner, et al. [20] determined the single boundary perturbation approach (SBPA) can also potentially provide less conservative buckling knockdown factors using a validated FEM.

The NASA Shell Buckling Knockdown Factor Project (SBKF) had the objective of aiding in the development of design-specific knockdown factors for launch vehicles by developing a validated modeling methodology using scaled sandwich composite cylindrical shells. Schultz, et al. [21] suggested that new knockdown factors could save 4% to 19% areal mass for sandwich composite launch vehicle structures. Four 2.4 m diameter sandwich composite cylinders were tested by NASA researchers as part of an effort to validate a finite element analysis approach to predict the buckling behavior. The buckling loads were predicted within 7% of the experiments [22–24].

In the present paper, the authors demonstrate a modeling methodology that successfully predicted the buckling behavior of a scaled launch-vehicle-like composite cylindrical shell. It is herein referred to as NASA-Delft Laminate 1 (NDL-1) with a layup based on a novel scaling methodology [25]. The goal of the scaling methodology is to produce a smaller-scale design which can mimic the buckling behavior of a large-scale launch-vehicle sandwich-composite buckling-critical composite shell. While this methodology has been demonstrated analytically and numerically, it is of interest to validate experimentally that the designs produced by the scaling methodology are buckling critical since the stacking sequences produced are nontraditional. Prior to the test, a detailed study to determine the most appropriate model parameters was performed. The high-fidelity model included details such as radial imperfections and thickness variations measured using a structured light scanning optical measurement system [26], and the material properties were characterized through coupon testing of the laminate. A detailed assessment is presented that compares the predicted prebuckling, buckling, and postbuckling radial displacements with low-speed and high-speed digital image correlation. Specifically, the paper describes in detail the buckling propagation over the 16.3 ms captured by the high-speed cameras as compared to the finite element analysis. The level of detail and modeling approach presented in this paper can be applied to large-scale buckling-critical composite launch vehicle structures.

The NDL-1 test article design and manufacturing is presented in Section 2. A summary of the as-built geometric imperfections and details of the finite element model used for pretest predictions are described in Section 3 and Section 4, respectively. The experimental setup is covered in Section 5. The results and discussion of Section 6 includes a comparison of the pretest predictions and posttest analysis correlation. Concluding remarks are given in Section 7.

2. Test article design and manufacturing

The test article, NDL-1, was manufactured from a carbon fiber-epoxy material system and had a nominal diameter of 800 mm, a nominal height of 1200 mm, and an acreage layup of $[23/0/-23]_{4s}$. The acreage layup was determined by a novel scaling methodology and was designed to fail in buckling. The analytical scaling methodology was used to determine a reduced-scale composite cylinder design that has a similar buckling behavior to a full-scale sandwich composite cylinder. This was achieved by matching the nondimensionalized parameters of the scaled design to the full-scale design [25]. The NDL-1 solid laminate design was a scaled-down version of the 2.4 m diameter sandwich composite cylinder, CTA8.1, which was designed and tested as a part of the SBKF [22]. The resulting designs from the scaling process are not constrained to common layup orientations, such as 0, 45, and 90 degrees, hence the unconventional design.

NDL-1 was a laminated composite cylindrical shell fabricated with 12.5-mm-wide unidirectional tows of Hexcel IM7/8552–1 (190 gsm), each 0.175 mm thick [27]. The in-plane lamina tensile and compressive elastic moduli (E), shear moduli (G), and Poisson's ratio (ν) for IM7/8552–1 lamina are listed in Table 1 [28]. Reference 27 provided failure stresses; therefore, failure strains were calculated assuming linear elastic behavior using the documented moduli and failure stresses. These failure stresses and calculated failure strains are reported in Table 2. The

Table 1
Nominal lamina properties of Hexcel IM7/8552-1 composite.

0-degree modulus	E_{11}	140.9 GPa
90-degree modulus	E_{22}	9.72 GPa
Shear modulus	G_{12}	4.69 GPa
Poisson's ratio	ν_{12}	0.356

Table 2
Documented lamina failure stresses [28] and calculated failure strains.

Direction	Failure Stress (MPa)	Failure Strain (με)
0-degree compressive	1731	−12,280
90-degree tensile	64	6584

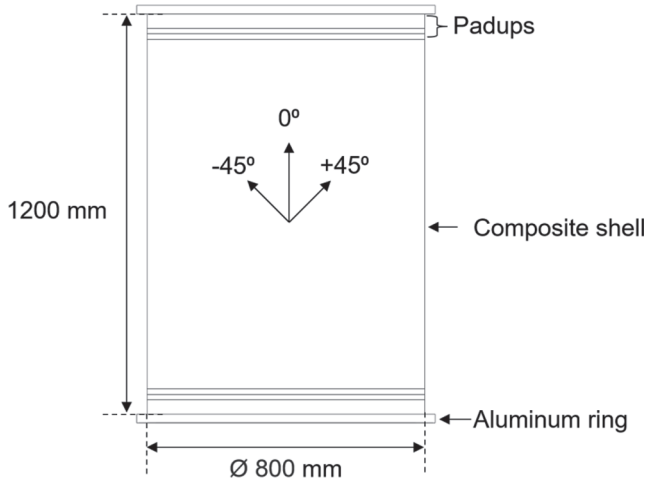

Fig. 1. NDL-1 geometry.

calculated strains were then used to confirm the buckling failure of NDL-1.

The test article was fabricated using the advanced fiber placement robot at the NASA Marshall Space Flight Center (MSFC) Composites Technology Lab. To manufacture the $[23/0/-23]_{4s}$ acreage layup, the unidirectional plies were laid on the outer surface of an aluminum cylindrical mandrel in the desired fiber orientation. The 0-degree direction is parallel to the longitudinal axis and the 90-degree direction is oriented circumferentially, or in the hoop direction. Additional plies, referred to as padups, were added at the ends of the test article to assist with load introduction. The test article weighed 20.68 kg. Its acreage and padup details are presented in Fig. 1 and Table 3. The padups consist of up to three plies — 90 degree, 45 degree, and −45 degree — that terminate sequentially near the ends. The 90-degree ply was the last ply to be dropped, closest to the midheight, followed by the 45- and −45-degree plies, respectively.

The unconventional layup led to some significant manufacturing challenges. To start, the laminate had a Poisson's ratio greater than 1.00. Also, the highly axially stiff layup and its associated coefficient of thermal expansion made it difficult to remove the composite cylinder from the aluminum mandrel; there was minimal clearance between the acreage section and the mandrel. A larger gap was present between the mandrel and the test article in the padup regions, potentially due to the presence of 0-degree and 90-degree plies.

After manufacturing, the ends of the composite cylinder were encased in an epoxy grout material to prevent brooming at the ends and to attempt to simulate clamped boundary conditions. The grout was 25.4-mm thick on each end and extended approximately 22.9 mm away

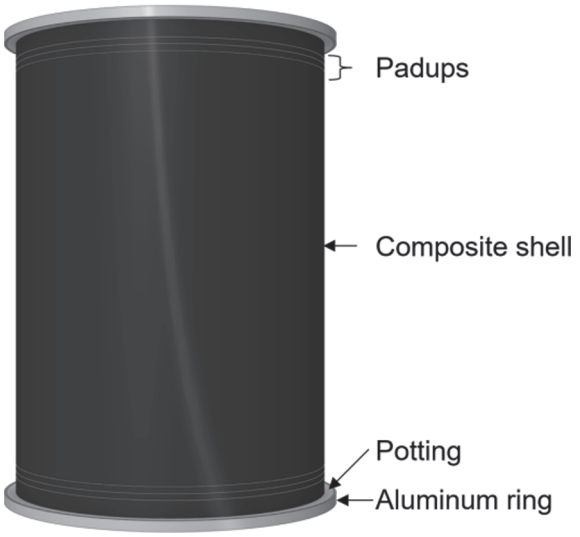

Fig. 2. 3D view of NDL-1 Assembly.

from the inner mold line (IML) and outer mold line (OML) surfaces of the composite cylinder. The innermost and outermost grout surfaces were encased with 6.35 mm thick aluminum rings. The ends of the test article were machined flat and parallel, with the shell exposed on either end to ensure uniform compressive load introduction directly into the test article, Fig. 2.

3. Measured geometric imperfections

After fabrication, the shape of NDL-1 was measured via structured light scanning to capture the radial position of the IML and OML surfaces. This data represents the as-built geometry of NDL-1. Structured light scanning is a photogrammetric technique used to capture the surface of the test article in a three-dimensional space. The IML and OML of the shell were scanned and combined in a single coordinate system to determine the radial location of the shell and its shell-end surfaces, along with thickness variations. The NDL-1 OML and IML radial locations are shown in Fig. 3a and Fig. 3b in an unrolled view. The blue colors correspond to a relatively inward position, while the red colors correspond to a relatively outward position. The radial position on the OML ranged from 406.60 mm to 403.58 mm. The radial position of the IML ranged from 401.10 mm to 399.35 mm. The average IML radial position was 400.23 mm and the nominal IML radius was 400 mm. A distinct feature can be observed in the OML and IML data, but it is more prominent in the IML: a band approximately 50 mm wide that extends around the entire circumference of the test article, centered approximately 150 mm above the midheight (0 mm). The aluminum mandrel on which NDL-1 was built was also structured light scanned, and this feature was present in the mandrel data. It was determined that this feature was an artifact of the surface machining process, and it was concluded that this mandrel feature was transferred to NDL-1 during fabrication. The thickness variations of NDL-1 are presented in Fig. 3c where the warmer colors correspond to thicker regions and the cooler

Table 3
Nominal NDL-1 acreage and padup layup details.

Region	Layup	Axial location from midheight (0 mm) of padup termination
Acreage	$[(23/0/-23)]_{4s}$	–
Padup 1	$[(23/0/-23)_{3s}/(23/0/-23/\overline{90})_s]$	+/−508.00
Padup 2	$[(23/0/-23)_{3s}/-\overline{45}/(23/0/-23/\overline{90})_s]$	+/−524.51
Padup 3	$[(23/0/-23)_{2s}/(23/0/-23/\overline{45})_s/-45/(23/0/-23/\overline{90})_s]$	+/−539.75

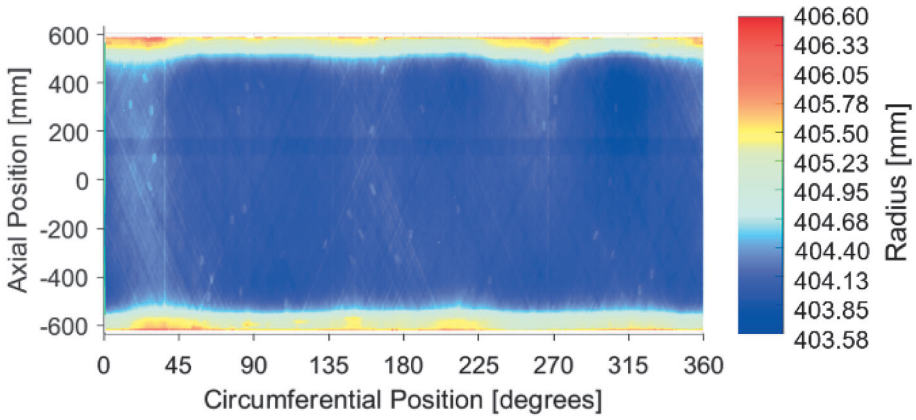

a. OML radial surface data.

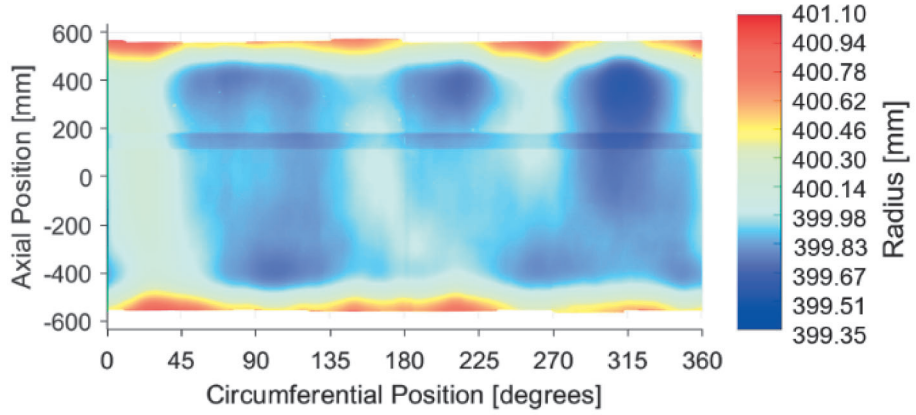

b. IML radial surface data.

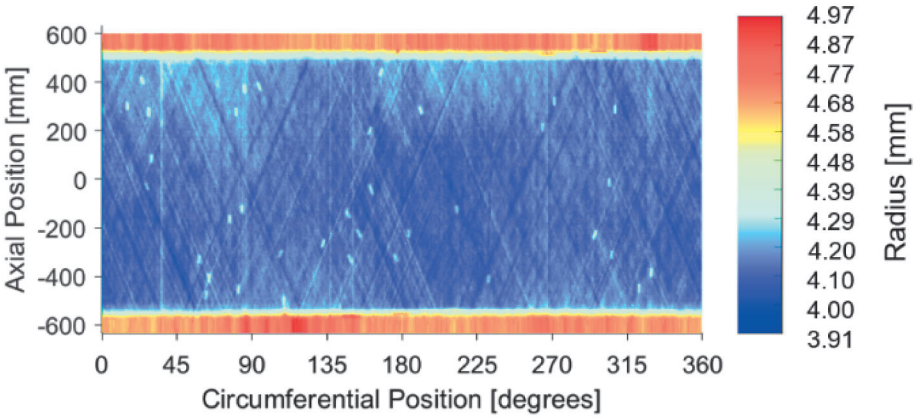

c. Interpolated thicknesses.

Fig. 3. NDL-1 radial and thickness imperfections.

colors denote relatively thinner regions. The diagonal pattern in Fig. 3c matches the 23-degree ply angle and corresponds to ply gaps and overlaps. Note that because structured light scanning output point cloud data, and the OML and IML spatial data points were not spaced at the same radial/circumferential positions precisely, the thickness plot shown in Fig. 3c was derived by interpolating the OML and IML radial data to regularly spaced axial and circumferential set. The interpolated IML data was subtracted from the interpolated OML data to give the shell's thickness profile. (The interpolated OML and IML were used in the FEM.)

In addition to the IML and OML surfaces, the top and bottom shell-end surfaces of NDL-1, which interface with the load frame, were also scanned. The data from the top shell-end surface is plotted in Fig. 4a, and data from the bottom end surface is plotted in Fig. 4b. The total variation in the top ring was 0.46 mm. The highest location was approximately 180 degrees from the lowest location. This was similar to the bottom

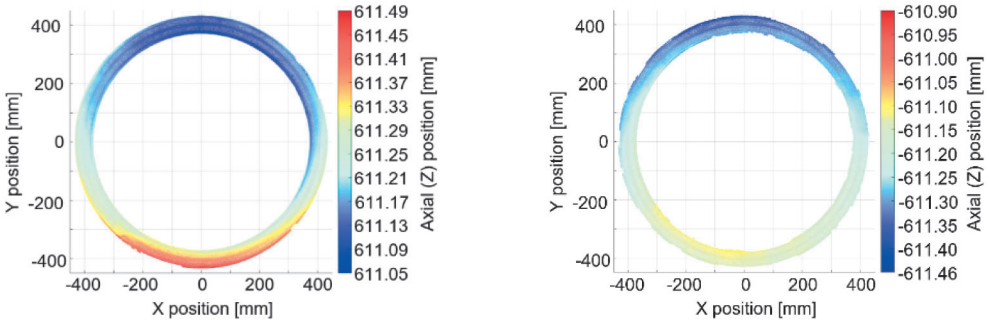

a. Top surface b. Bottom surface

Fig. 4. NDL-1 axial position of top and bottom shell end surfaces.

surface, but the bottom surface had a maximum imperfection amplitude of 0.44 mm. Capturing this data is important in assessing the effects of nonuniform loading in the finite element model.

4. Finite element model and analysis

The finite element program used for the pretest predictions and posttest analysis correlation was Abaqus 2017 [29]. The modeling and analyses were performed at the Delft University of Technology. Prior to developing the finite element model to predict the buckling load and behavior of NDL-1, an investigation was conducted and documented to understand the effect element type and mesh size have on the buckling response. Also, this section presents a discussion of the laminate material property characterization that was used in the finite element model for the pretest predictions and posttest analysis correlation. Finally, analysis parameters of the implicit dynamic analysis used for the predictions are presented.

4.1. Element type and mesh size selection

A finite element model (FEM) of NDL-1 with nominal geometry was used to investigate two element types to model the composite test article: the S4R four-node conventional shell element and the SC8R eight-node continuum shell element. The former was modeled with two-dimensional geometry and contains rotational and displacement degrees of freedom, while the latter was modeled with three -dimensional geometry and only contains displacement degrees of freedom. Both elements allow transverse shear deformations, and both are suitable for geometric nonlinear problems [28]. With the SC8R element, only one element through the thickness was used.

A mesh convergence study was completed with both the S4R and SC8R elements by comparing the linear eigenvalue buckling loads. The results are presented in Fig. 5 for mesh sizes of 50 mm, 25 mm, 20 mm, 10 mm, 7.5 mm, and 5 mm. This corresponds to approximately 1100, 4500, 7000, 28,000, 50,000, and 112,000 elements, respectively. In the figure, the predicted linear buckling loads for the S4R and SC8R elements, dashed and solid lines, respectively, begin to converge and plateau at a mesh size of 10 mm (approximately 28,000 elements). Ultimately, a mesh size of 5 mm (approximately 112,000 elements) was selected to better capture the imperfection signatures of the OML and IML. The 5 mm mesh size is approximately 0.7 elements per degree around the circumference.

Both linear eigenvalue and nonlinear dynamic analyses were performed to assess S4R and SC8R elements with the 5 mm mesh size. There is less than a 1% difference between the linear eigenvalue buckling loads of the S4R and SC8R models, 2284 kN and 2295 kN, respectively. Additionally, the linear eigenvalues for both element types are within 1% or less of the analytical buckling load of 2271 kN calculated using Equation (1), where Nx is the buckling load per unit length, l is the length of the cylindrical shell, m is the number of axial halfwaves, and the matrix A corresponds to the laminate stiffness. Matrix A is a function of m and n (number of circumferential waves) [17]. The critical number of m and n is 9 and 0, respectively. This was determined by minimizing Equation (1) with respects to m and n. The buckling mode shapes for the two element types are also very similar for the first mode as seen in Fig. 6. The predicted buckling loads for each element type for the eigenvalue and nonlinear dynamic analyses are listed in Table 4.

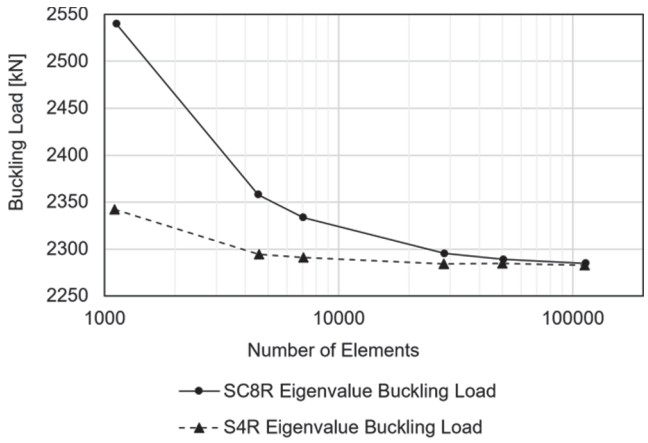

Fig. 5. The eigenvalue buckling load for S4R and SC8R shell models versus the number of elements.

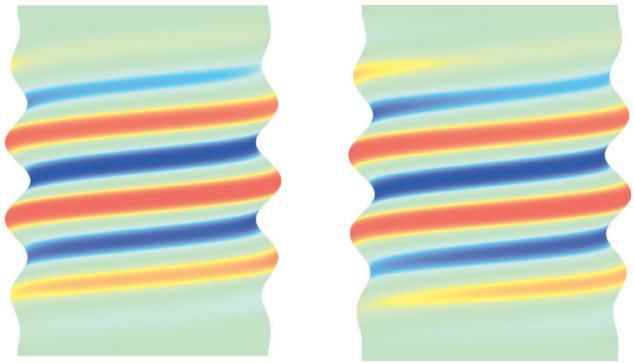

a. S4R elements b. SC8R elements

Fig. 6. First buckling mode shapes.

Table 4
Buckling loads determined by eigenvalue analysis and nonlinear dynamic analysis for S4R and SC8R elements.

Element	Eigenvalue Analysis[kN]	Nonlinear Dynamic Analysis[kN]
S4R	2284	2193
SC8R	2295	2194
Difference	−0.4%	≈ 0%

$$N_x = \left(\frac{l}{m\pi}\right)^2 \frac{\begin{vmatrix} A_{11} & A_{12} & A_{13} \\ A_{21} & A_{22} & A_{23} \\ A_{31} & A_{32} & A_{33} \end{vmatrix}}{\begin{vmatrix} A_{11} & A_{12} \\ A_{21} & A_{22} \end{vmatrix}} \tag{1}$$

In addition, the buckling loads predicted from nonlinear dynamic analyses using both element types were nearly identical (1 kN difference, or well within 1%). Given that both element types predicted similar behaviors, the SC8R was selected for compatibility with in-house imperfection-processing software. Nodal coordinates of the SC8R elements were manipulated to match the surface positions of the OML and IML data. Moving the OML and IML nodes accounts for the thickness variations by default. In contrast, S4R elements would have required midsurfacing the IML and OML data, along with individual element-by-element thickness assignments.

While the composite cylinder was modeled using SC8R elements, the potting material and aluminum rings were modeled with C3D8 three-dimensional brick elements. A detailed view of the FEM is shown in Fig. 7. The yellow-orange color corresponds to the continuum shell elements with properties for padup 3. The blue color represents the continuum shell elements with properties for padup 2, the red corresponds to padup 1, and the cyan represents the acreage. The potting is represented by the purple color, and the aluminum rings are gray.

4.2. Material properties

Laminate coupon testing was completed before the test of NDL-1 to characterize the laminate stiffness of its unconventional layup, $[23/0/-23]_{4s}$. Seven tensile coupon specimens, nominally 24.5 mm wide and 4.32 mm thick, were built with the same layup as NDL-1. A summary of the longitudinal laminate modulus, Poisson's ratio, width, and thickness from the seven tested specimens is shown in Table 5. The coupon specimens were 4.3% thicker than the average acreage thickness of the test article. The average cured ply thickness was 0.180 mm for the coupon specimen, and 0.173 mm for the test article. Due to the thickness discrepancy, two different assumptions were made when extrapolating resultant ply properties from the coupon test to the test article and its FEM. The first was that the coupon specimen and test article had the same constant fiber volume fraction. The second assumption was that the number of fibers per unit area was the same in the coupon specimen and the test article. In this case, it was assumed the number of fibers remained constant per unit area, but excess resin bled off during the cure cycle of the test article, thereby causing the thickness discrepancy. The intent of creating two sets of material properties was to bound the response of NDL-1 since there are more potential sources of variation when manufacturing with unidirectional tows.

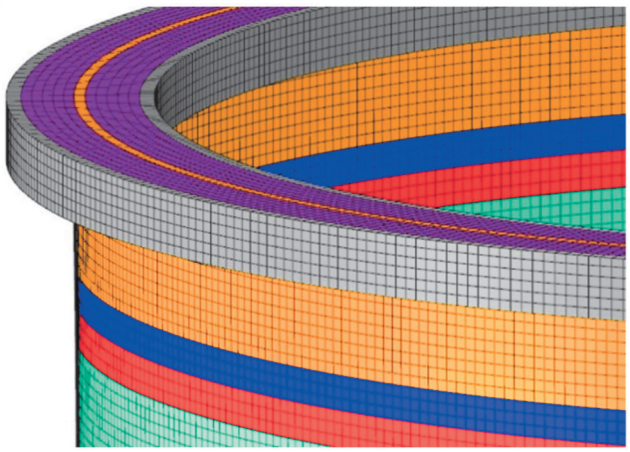

Fig. 7. FEM details.

Using the data from the tensile tests, the associated local fiber-direction (E_{11}) and transverse (E_{22}) lamina stiffnesses to be used in the FEM of NDL-1 were determined through a virtual coupon test. The nominal tensile specimen was modeled using SC8R elements and the nominal lamina E_{11} and E_{22} properties of Table 1 as an initial guess. They are reported in the first row of Table 6 for comparison and are called the "nominal properties". The lamina moduli E_{11} and E_{22} were modified in the finite element program until the predicted laminate's *overall* longitudinal stiffness and Poisson's ratio from the virtual tensile test matched the corresponding mean values from the coupon tests (108.7 GPa and 1.29, respectively) within 1%. Those E_{11} and E_{22} properties, the second row of Table 6, satisfy the assumption that the test article and coupon specimens had the same fiber volume fraction.

To consider the second assumption of a constant quantity of fibers per unit area, the E_{11} and E_{22} values previously determined were modified to account for the difference in thickness between the coupon specimens and NDL-1. It was presumed that the number of fibers in one tow should remain constant even after cure. This implied that the 0.173-mm-thick tow should have a similar load–displacement behavior as the 0.18-mm-thick tow. Therefore, the reduction in cross-sectional area should result in an increase in stiffness. To account for this, the constant-quantity-of-fibers E_{11} and E_{22} moduli were increased proportionally to account for the 4.3% thickness difference. Those E_{11} and E_{22} moduli are reported in the third row of Table 6. The shear moduli were not adjusted because these have little influence on the laminate properties.

Two different finite element models were developed, one with the constant-fiber-volume-fraction moduli and one with the constant-quantity-of-fibers moduli. These models will be referred to as the pre-test prediction models. The potting was modeled assuming isotropic material properties with an elastic modulus of 7.58 GPa and a Poisson's ratio of 0.3. The aluminum ring was modeled with an elastic modulus of 69.00 GPa and a Poisson's ratio of 0.33.

4.3. Analysis

Nonlinear implicit dynamic analyses were performed to predict the prebuckling, buckling, and postbuckling response of NDL-1 using the constant-fiber-volume-fraction assumption and the constant-quantity-of-fibers assumption. To apply the displacement, a single reference node in the center of the test article at the top was connected to the top edge nodes of the test article, potting, and aluminum ring through tie constraints. The top reference node had all degrees of freedom constrained except for the axial direction. The bottom of the test article was similarly tied to a reference node centered at the bottom edge of the cylinder using the same technique. All degrees of freedom associated with the bottom reference point were fixed.

A total displacement of 2.5 mm was applied to the top reference node at a rate of 2 mm per minute in the axially compressive direction. The total displacement was divided into two steps. The first step, or prebuckling step, was a dynamic analysis that specified 0.12 s for the initial and maximum increment. The second step of the analysis began after a time period of 60 s. The load rate remained constant, but the initial and maximum increments were decreased to 0.009 s. This defined the buckling phase of the analysis. The larger time step in the prebuckling phase was to increase computational efficiency. The smaller time step was employed during the buckling step to ensure the peak load was captured accurately and to have a detailed understanding of the

Table 5
Summary of NDL-1 laminate tensile test data.

Specimen Number	1	2	3	4	5	6	7	Mean
Longitudinal modulus [GPa]	107.3	108.7	115	109.4	106.1	108.8	105.3	108.7
Poisson's ratio [-]	1.24	1.29	1.29	1.28	1.27	1.31	1.35	1.29
Width [mm]	25.3	25.4	25.4	25.4	25.4	25.4	25.4	25.4
Thickness [mm]	4.32	4.32	4.32	4.34	4.32	4.39	4.32	4.32

Table 6
Nominal, constant fiber volume fraction and constant quantity of fibers material-properties.

Property Set	E_{11} [GPa]	E_{22} [GPa]	G_{12} [GPa]	ν_{12} [-]
Nominal	140.9	9.72	4.69	0.356
Constant fiber volume fraction	152.2	8.75	4.69	0.356
Constant quantity of fibers	158.7	9.12	4.69	0.356

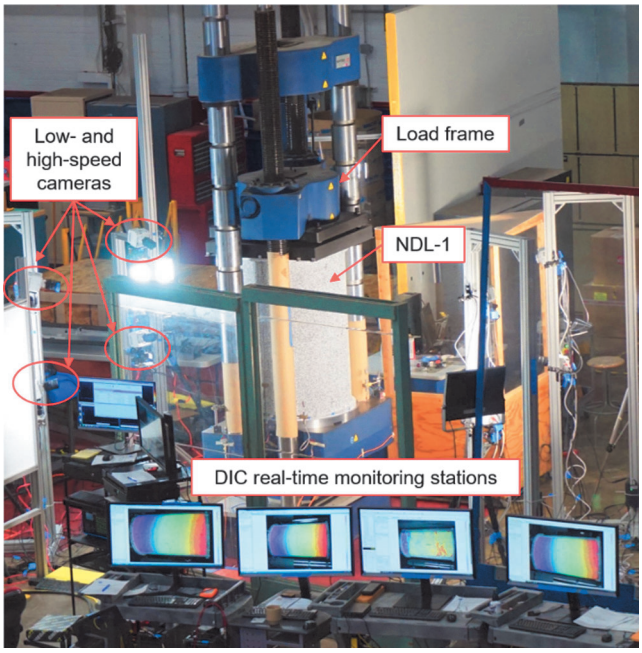

Fig. 8. NDL-1 experimental setup at NASA Langley Research Center.

predicted buckling progression. This combination of steps allowed the analysis to be reasonably computationally efficient, while still obtaining the desired buckling data.

5. Experimental setup

Test article NDL-1 was tested in axial compression at NASA Langley Research Center using a load frame which is capable of applying up to 3000 kN. In the compression loading set up, the top platen was fixed and the test article was compressed by the bottom platen, actuated by a hydraulic system. The experimental setup is shown Fig. 8. Three subcritical load sequences — in which failure was not expected — were planned before the final test to failure. The subcritical load sequences consisted of loading NDL-1 in pure axial compression at levels that were 20%, 40%, and 60% of the test article's predicted linear bifurcation load, 2295 kN. A displacement-controlled compression rate of 0.08 mm/min was applied for all load sequences.

Test data was obtained from several instrumentation sources. The load was measured via a load cell. Displacement was measured by six direct current differential transducers (DCDTs) positioned around the load frame, Fig. 9. Strain was measured with 32 electrical resistance strain gages as shown in Fig. 10. The OML gauges were odd numbers, and the IML gauges were even numbers. On both the IML and OML surfaces, 12 axially oriented gauges were spaced at 0, 90, 180, and 270 degrees around the circumference with axial positions of −562 mm, 0 mm (midheight), and 562 mm. These gauges were designated with an "A" which references the axial direction. Additionally, four inner and four outer midheight gauges measured hoop strain at 0, 90, 180, and 270 degrees. These gauges were designated with an "H" which references the hoop direction.

Eight digital image correlation (DIC) systems were used to observe the experiment: four low-speed systems and four high-speed systems, with each system comprised of two cameras in a stereo configuration. The low-speed data was captured at a rate of 1 frame per second. The lenses and standoff distances were selected such that the system's resolution was optimize for the desire field-of-view, i.e. maximum spatial resolution. The high-speed data was captured at rate of 20,000 frames per second. The outer surface of the test article, which included the composite cylinder and the aluminum ring containing the potting, had a high-contrasting speckle pattern applied for DIC as seen in Fig. 8. The ideal speckle diameter for the low-speed system was generally between 4 and 6 pixels. However, the speckle pattern diameter was doubled to 8 to 12 pixels/speckle for the low-speed systems to accommodate the lower resolution of the high-speed cameras, because the latter's chosen resolution was lower than the former's. This translated to a speckle size ranging from 4.5 mm to 6 mm.

Low-speed and high-speed camera pairs were positioned facing the circumferential positions of the shell at 45, 135, 225, and 315 degrees as indicated in Fig. 11. The fields of view for the DIC systems were centered on the NDL-1 midheight. Low-speed DIC recorded throughout the entire test. Prebuckling radial and axial displacements were generated from this data. High-speed DIC was used to capture the buckling event (initiation and propagation). Real-time monitoring stations were used to observe full-field displacements and strains from low-speed DIC along with load and axial displacements during the test.

The top load platen was balanced to help ensure even load introduction before the first load sequence. The top load platen system consisted of the two black plates located above NDL-1 in Fig. 8. Between the two plates was a hemispherical joint that was centered in the middle of the plates. To balance the top load platen, the readings for the eight back-to-back strain gauges placed every 90-degrees on the top end of the test article must be within 10% of each other. Virtual extensometers within the DIC software were also utilized to examine the load introduction in areas where strain gages were not present. Based on the virtual extensometer data, the top shell-end surface was shimmed between the 210-degree and 315-degree circumferential locations to allow for a more uniform load introduction.

6. Results and discussion

A comparison of the data derived from pretest prediction models as described in Section 4 and the experimental data is presented. First, a comparison of the load versus displacement data is described. Next, the axial and circumferential membrane strains are compared. Then the radial contour plots generated from the low-speed DIC data are compared against the FEM predictions for the prebuckling response and incipient buckling behavior. Finally, the postbuckling response as measured by the high-speed DIC data is presented.

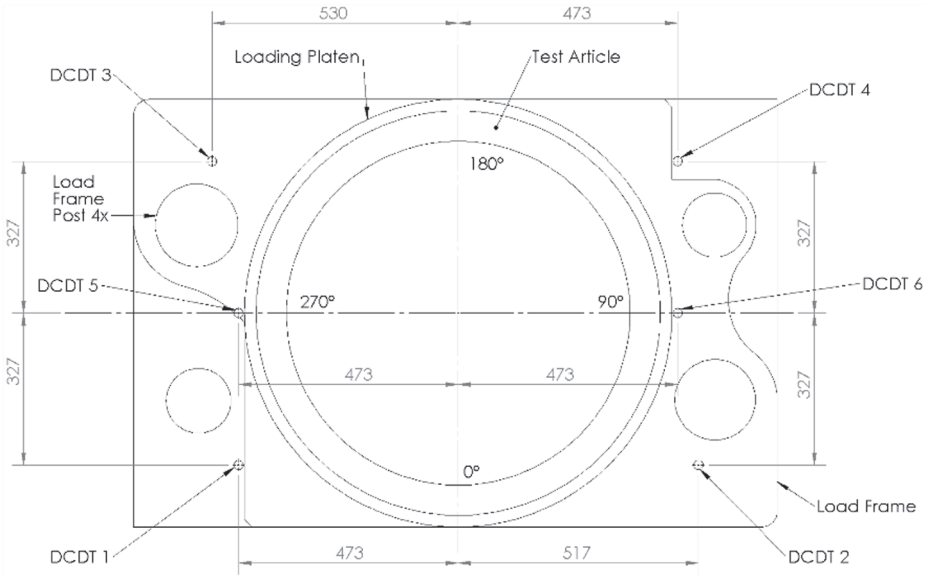

Fig. 9. Midsection top-view drawing of the load frame indicating angular locations and DCDT mounting points. All dimensions are in millimeters.

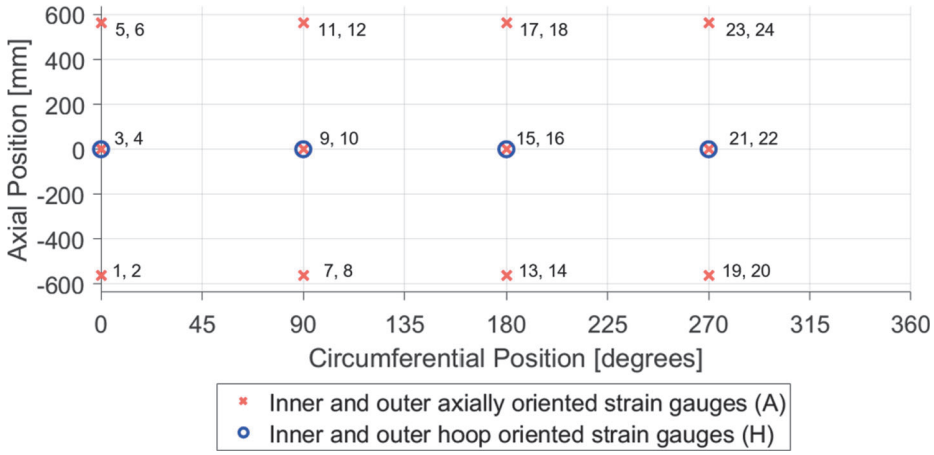

Fig. 10. Strain gauge locations and orientations on the shell and gauge number.

6.1. *Pretest prediction models and test data comparison*

During the test-to-failure load sequence, NDL-1 failed at a peak load of 2077 kN and a total axial displacement of 2.19 mm. The overall behavior of the test article matched the pretest predictions well for both models, — constant-fiber-volume-fraction and constant-quantity-of-fibers — as seen in the load versus displacement plot of Fig. 12. The black line corresponds to the test data in which the average axial displacement was derived from the low-speed DIC data. Both pretest prediction models contained the measured radial and thickness imperfections (Fig. 3), and top and bottom shell surface imperfections (Fig. 4). The blue line represents the pretest predictions for the material properties assuming a constant fiber volume fraction as described in Section 2. The orange line represents the pretest predictions using the same measured imperfections but assumes a constant quantity of fibers per unit area. Both models show good correlation, but the constant-fiber-volume-fraction model matches the test data better by predicting a buckling load of 2075 kN, a 0.04% difference from the test. The constant-quantity-of-fiber model predicted a buckling load of 2154 kN, a 3.7% difference. There is a 0.2% difference in stiffness between the constant-fiber-volume-fraction model and the test data, and a 3.7% difference between the stiffness of the constant-quantity-of-fibers model and the test data. Since the constant-fiber-volume-fraction model correlated better, those results are presented herein.

The intent of the shims was to improve load uniformity. The influence of the end conditions was assessed by also running a model without the shell-end imperfections. There was no difference between the models. The responses predicted for models with and without the shell-end imperfections were nearly identical. Therefore, a single model, the model with shell-end imperfections, is presented herein.

The back-to-back axial (A) membrane strains, or the average strain of the IML and OML gauge, at the top, midheight, and bottom of NDL-1 for the test and FEM, are shown in Fig. 13. The measured axial membrane strains remain essentially linear up to the buckling load of 2074 kN. This is also apparent in the FEM data as well. There is more divergence in the membrane data at the top than there is at the midheight and bottom.

The top, +562 mm axial location, axial membrane strains calculated from the test data at buckling at 0-degrees (5A/6A) and 180-degrees (17A/18A) were −1673 με and −1704 με, respectively. The calculated axial membrane strains from the FEM at those locations were −1546 με and −1558 με, respectively, which are 8% less than the predicted. The axial strains calculated from the test data just prior to buckling for the 90

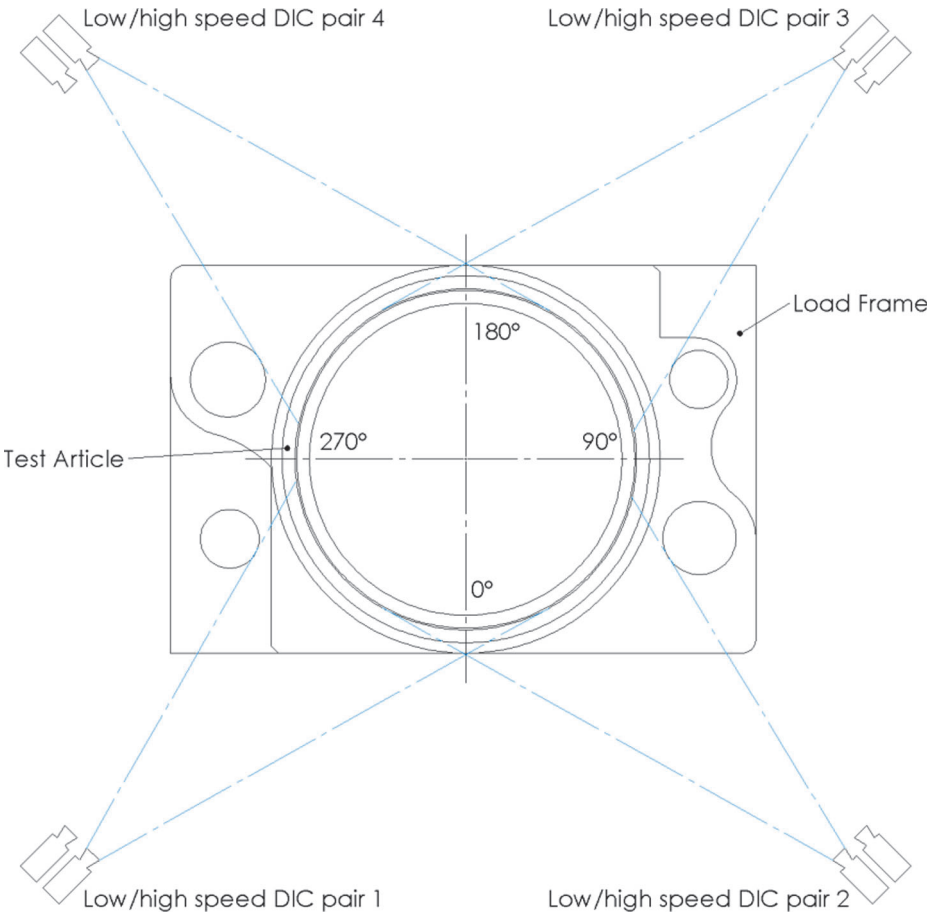

Fig. 11. Locations of DIC systems. Approximate fields of view are indicated by blue lines.

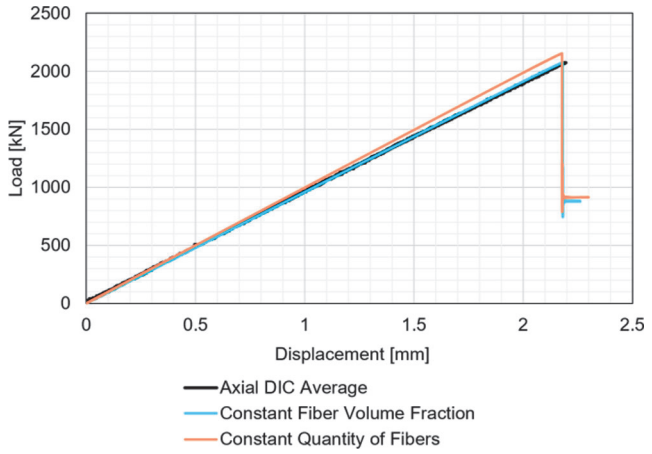

Fig. 12. Load versus average displacements plot.

degrees (11A/12A) and 270 degrees (23A/24A) circumferential locations were overpredicted by more than 4%. The calculated membrane strain from the test data and from the FEM for gauges 11A/12A were −1504 με and −1568 με, respectively. The calculated axial membrane strains from the test data and predicted strains for 23A/24A were −1473 με and −1568 με, respectively. The higher-than-predicted strains at the 90- and 270-degree circumferential locations indicates potential high spots on the loading surface in those regions. This may be associated with the shims placed between 210- and 315-degrees while balancing the top load platen. It should be noted that these strains are well below the calculated longitudinal compressive failure strain of −12,280 με listed in Table 2.

It is apparent that the effects of nonuniform loading began to attenuate as the load was distributed down the height of the test article. The percent difference between the membrane strains calculated from the FEM and from the test data at buckling at the midheight, 0-mm axial position, (Fig. 13b) are less than at the top. For example, the calculated FEM axial membrane strain at buckling at midheight at the 0-degree circumferential location (3A/4A) and 180-degree (15A/16A) circumferential locations were −1933 με and 1941 με, respectively. These values are approximately 3% less than the calculated axial membrane strains from the test data at buckling which were −1990 με for gauges 3A/4A and −2010 με for gauges 15A/16A. As with the top membrane strains, the 0-degree and 180-degree membrane strains were overestimated, and the 90-degree and 270-degree circumferential locations were underestimated. The FEM-calculated membrane strains for gauges 9A/10A were −1932 με and 21A/22A was −1908 με. The membrane strains calculated from test data for those respective locations were −1853 με and −1823 με, which are 5% less than the FEM-calculated axial membrane strains. Also, the strains calculated from the test data at buckling are lower than the calculated compressive longitudinal failure strains listed in Table 2.

Similar trends to the top and middle calculated membrane strains are noted when comparing the axial membrane strains from FEM data and test data at the bottom, −562 mm axial position, of NDL-1 (Fig. 13c) at the buckling load. The calculated predicted strains at buckling for the gauges at 0 degrees (1A/2A) and 180 degrees (13A/14A) were −1588 με and −1580 με. The calculated axial membrane strains from the test data at those respective locations were −1608 με and −1617 με. There was

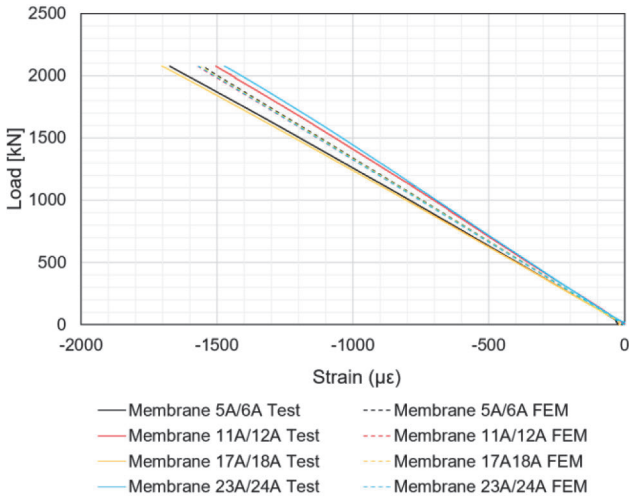

a. Top membrane strains

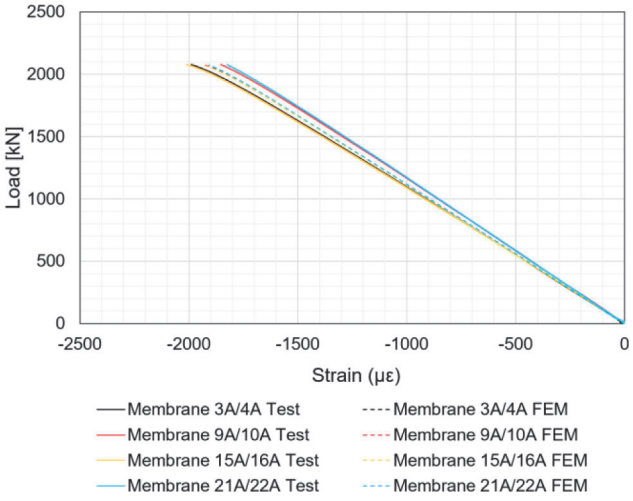

b. Midheight membrane strains

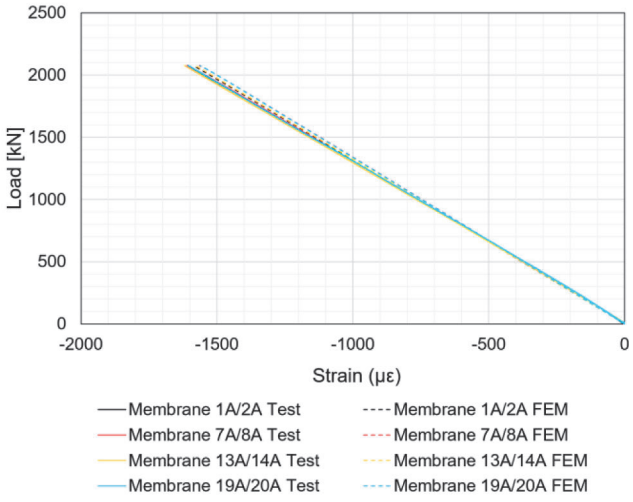

c. Bottom membrane strains

Fig. 13. Axial membrane strain for the pretest predictions (FEM) and test.

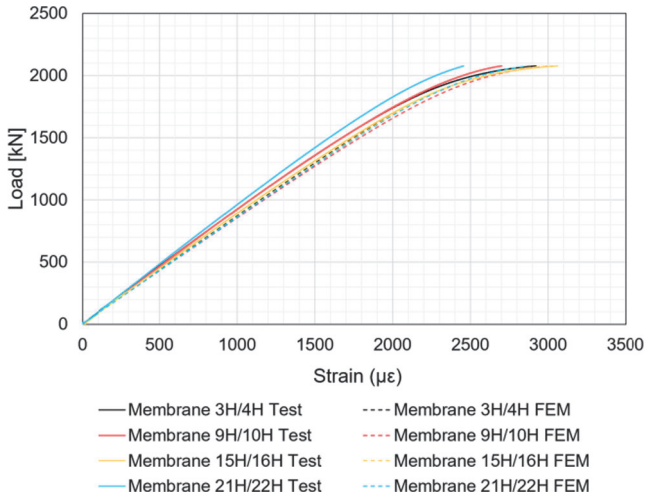

Fig. 14. Hoop membrane strain for the pretest predictions (FEM) and test.

less than a 3% difference between these values. There is also a 3% difference between the calculated strains from FEM and test data for the gauges at 90- and 270-degree circumferential locations (7A/8A and 19A/20A). The membrane strains calculated at the buckling load from FEM data were −1565 με and −1562 με, and the calculated membrane strains from test data at buckling were −1610 με and −1606 με, respectively. These values are also less than the failure strains reported in Table 2.

The hoop membrane strains at midheight calculated from the FEM and test data show signs of nonlinearity approaching the peak load, Fig. 14. This is attributed to the large out-of-plane deformations that occur just prior to and during a buckling event. While a similar curve shape is presented for the measured data and the predicted data, the predicted and measured circumferential strains diverge from the beginning with the predicted circumferential strains typically being less than the observed. The FEM indicates that all calculated membrane hoop strains at 0, 90, 180, and 270 degrees generally have the same slope. This remains true for all membrane hoop strain gauges except for the those determined from gauges 21H/22H at the 270- degree locations. This is consistent with the observation made in the axial membrane data. The maximum predicted membrane hoop strain was 3053 με for gauges 3H/4H at the 0-degree circumferential location. The

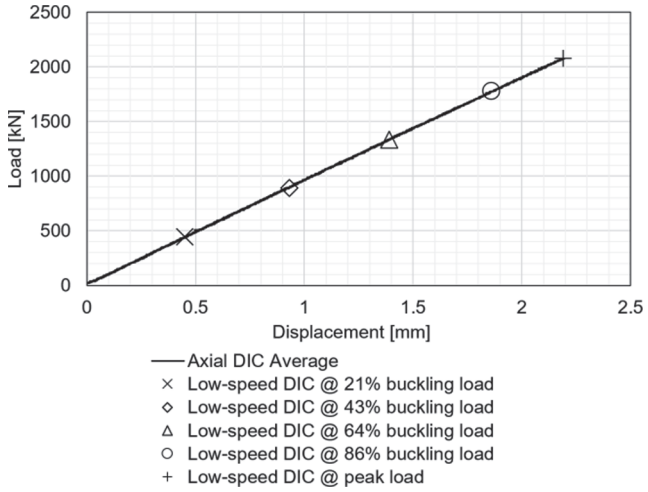

Fig. 15. Load versus axial displacement from DIC, with markers indicated by symbols corresponding to Fig. 16 through Fig. 20.

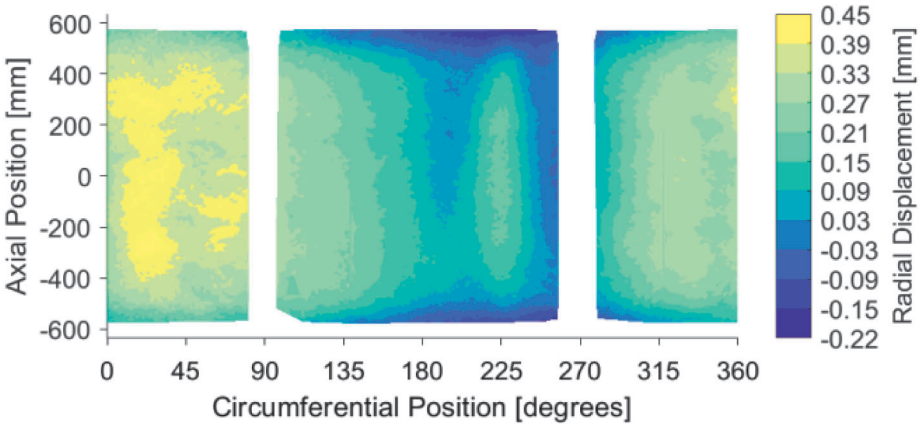

a. Experimental data

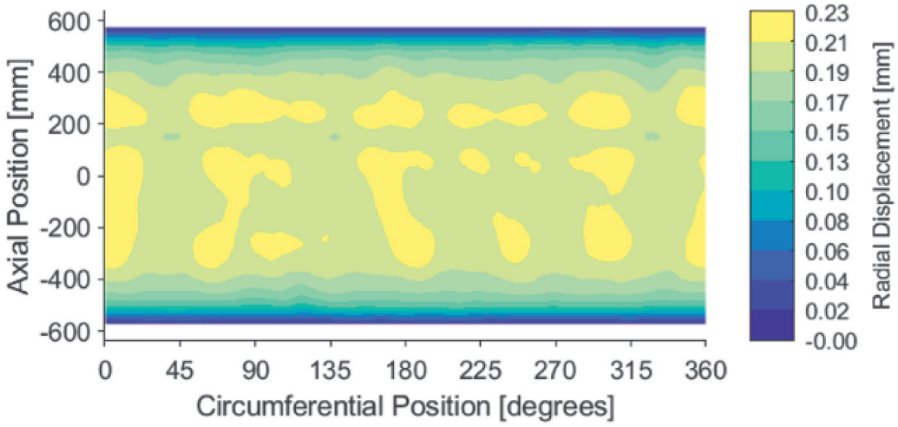

b. FEM data

Fig. 16. Radial displacement at 21% of the experimental buckling load.

maximum observed membrane hoop strain was 3060 με for gauges 15H/16H at the 180-degree circumferential location. These values are also well below the calculated transverse tensile failure strain of 6584 με, as reported in Table 2.

The radial displacement contours for the test and from the pretest prediction model are presented for the prebuckling, incipient buckling, and postbuckling response. The DIC cameras were not able to measure data over the entire OML because of interference from the load-frame posts; therefore, no full-field strain and displacement data was captured around the 90-degree and 270-degree circumferential locations. The low-speed DIC cameras captured the prebuckling response, while the high-speed DIC cameras captured the postbuckling response.

The low-speed DIC systems primarily captured the state of the test article prior to and at incipient buckling. Fig. 15 shows the experimental load versus displacement plot with markers corresponding to 21%, 43%, 64%, 86% and 100% of the experimental buckling load, intervals of 445 kN. These markers relate to Fig. 16 through Fig. 20 where the associated radial deformation contours are presented at the specified load levels.

Starting at a load level of 21% of the experimental buckling load, it can be seen that the test article had a greater radial displacement than what was predicted by the FEM, Fig. 16. The maximum measured outward radial displacement was 0.45 mm while the predicted was 0.23 mm. The shape of the outward radial deformation in the finite element model was relatively uniform, where the radial deformation predicted in the acreage region ranged from 0.23 mm to 0.21 mm. On the contrary, the test article exhibited an oval-shaped pattern. The maximum outward radial deformation occurred around 22.5-degrees with a magnitude of approximately 0.45 mm. The relative inward deformation exhibited by the test article was −0.22 mm. There was no inward radial deformation predicted by FEA. Also, it should be noted that a band appeared between +100 mm and +200 mm in the predicted response, Fig. 16b. This coincides with the feature on the mandrel in the radial displacements plot in Fig. 3a and Fig. 3b, but it does not appear in the test data at this load level, shown in Fig. 16a.

Trends similar to those observed at 21% of the experimental buckling load were also observed at 43% of the experimental buckling load, Fig. 17. The outward displacements were underestimated by the model with a predicted maximum displacement of 0.46 mm, but the maximum outward displacement observed was 0.69 mm. The minimum inward deformation is also underestimated because no inward displacement was reported in the FEM data, but the test article maintained its relative inward deformation of −0.22 mm. More distinct circumferential wave features began to develop in the experimental data, which correlates better with the predicted response, but the ovalization was still apparent. The mandrel feature that was observed in the predicted radial deformation plots at 21% of the experimental buckling load, began to appear in the experimental data at 43% of the experimental buckling load.

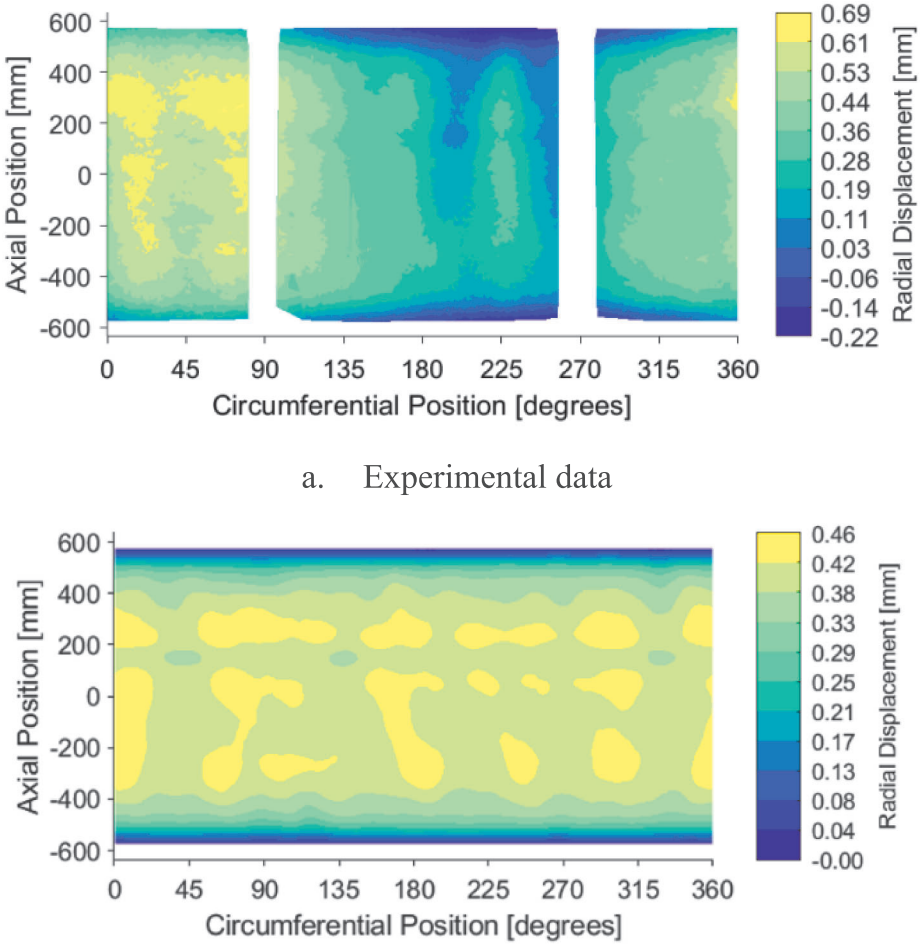

Fig. 17. Radial displacement at 43% of the experimental buckling load.

At 64% and 86% of the experimental buckling load, more defined dimples began to form in both the FEM and experimental data. Most notable was that a band of circumferential waves was witnessed between +100 mm and +200 mm, as indicated in Fig. 18 and Fig. 19. As the applied load increased, the outward radial deformation increased from 0.70 mm to 0.97 mm in the FEM data. However, no additional inward radial deformation or growth was predicted. With the experimental data, the test article exhibited an increase in outward deformation from 0.99 mm to 1.30 mm. The observed minimum inward deformation remained relatively consistent from 64% to 86%. An inward displacement of −0.27 mm at 64% of the experimental buckling load was noted in Fig. 18a. The observed inward deformation at 86% of the experimental buckling load was −0.25 mm, Fig. 19a. No inward deformation was witnessed in the FEM pretest predictions for either load level.

Just prior to buckling, more elements of agreement began to appear between test and analysis with regards to the general shape. Inward dimples started to form and concentrated on the mandrel imperfection feature between axial positions +100 mm and +200 mm, Fig. 20. The predicted response from the FEM had four dimples spaced 45-degrees apart beginning at 0-degrees between the +100 mm and +200 mm axial positions, which were considered potential failure locations. The test data shows that a single dimple began to dominate the radial deformation plot at the same axial position predicted, +100 mm to +200 mm, at the 200-degree circumferential location. The maximum inward displacement observed in the test was −0.35 mm, while a maximum inward deformation of only −0.04 mm was predicted.

Notably, the growth of the maximum outward radial deformation and minimum inward displacements was relatively consistent between load levels for the experimental data and FEM data. For example, the change in the maximum outward deformation observed in the experimental data between 21% and 43% of the experimental buckling load was 0.23 mm. The test article did not exhibit any change in the inward deformation. Similarly, the difference between the maximum outward deformation in the FEM data from 21% to 43% of the experimental buckling load was 0.24 mm. There was also no predicted change in the minimum inward deformation. From 43% to 64% of the buckling load, the experimental data showed a change in maximum outward deformation and minimum inward deformation as 0.30 mm and −0.05 mm, respectively. For the FEM radial deformations, these same quantities correspond to 0.24 mm and 0.00 mm. The growth in maximum outward displacement from 64% to 84% of the experimental buckling load was 0.31 mm as exhibited by the test article and FEM data showed 0.27 mm. The change in inward radial deformation at the same load level from the experimental data was +0.02 mm and no change in the FEM data. Finally, the growth in maximum displacement from the experimental data from 86% of the experimental buckling load to just before buckling was 0.45 mm as, and 0.36 mm as output by the FEM. The growth of

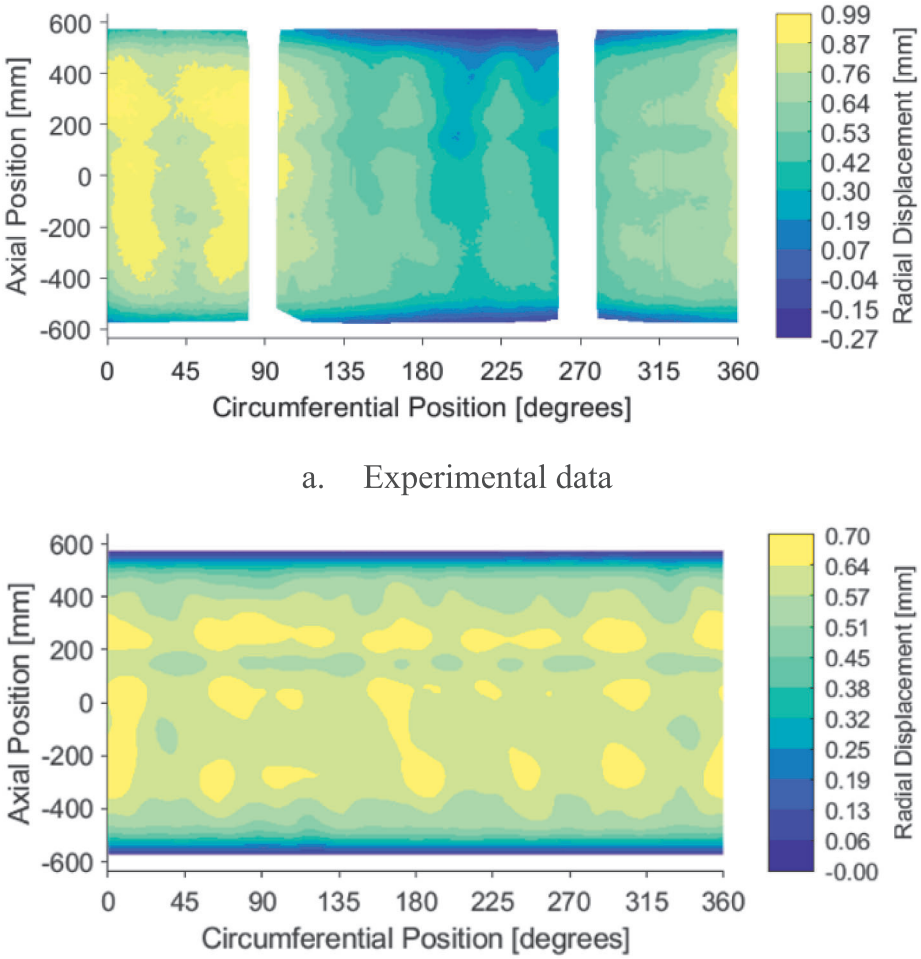

Fig. 18. Radial displacement at 64% of the experimental buckling load.

inward deformations as seen in the experimental data was −0.10 mm, and the FEM was −0.04 mm. These subtle changes between load levels are averaged out if just comparing the outward radial displacement at 21% of the experimental buckling load and just prior to buckling for the experimental data and the FEM data which is 1.21 mm for both. The overall magnitudes of the radial displacements were not consistent between the experimental data and FEM data, but the overall growth of radial deformations between load steps is similar.

The buckling initiation and post buckling response were recorded with 4-pairs of high-speed cameras with a capture rate of 20,000 frames per second. The buckling propagation can be observed in a series of images from the first high-speed image through 16.3 ms after the first image was taken (Fig. 21a–Fig. 21d). Buckling initiated at a dimple center at about the 200-degree circumferential location with an inward radial deformation of −3.10 mm, as seen in Fig. 21a. According to the images, it took approximately 7.3 ms for the buckling to fully propagate around the circumference of the test article, as shown in Fig. 21a–Fig. 21c. In the 7.3 ms from Fig. 21a to Fig. 21c, the buckling initiation dimple went from −3.10 mm to −33.25 mm of radial deformation. The pattern observed in Fig. 21b consists of two axial half waves and seven circumferential full waves. Then the postbuckling pattern transitioned from seven to six circumferential half-waves, Fig. 21d. As the pattern evolved, the radial displacements grew significantly. The postbuckled equilibrium radial deformation determined from analysis (Fig. 22) was seven circumferential waves and two axial half-waves, one circumferential wave more than in the final high-speed image (Fig. 21d).

Posttest inspection of the test article revealed a shallow delamination that was observed approximately at midheight and a circumferential location of 170-degrees. The delamination was approximately 152 mm in length and 51 mm in width as indicated by the red outline in Fig. 23. It is believed the delamination occurred during the dynamic buckling event. The delamination seems to have occurred at an inflection point between the inward dimple where buckling initiated and the adjacent outward dimple as seen in Fig. 21a. The angle of the delamination is +23-degrees which is the angle of the outer most ply. The difference between the predicted and observed postbuckling behavior may be attributed to the delamination. The delamination caused a localized stiffness differential that was not accounted for in the FEM.

Though NDL-1 was designed to fail in buckling, this should be confirmed especially with the damage observed after failure. The axial strain and hoop strain at the failure location derived from DIC is plotted in Fig. 24a and Fig. 24b. The axial strain in the center of the dimple, where buckling initiated, was −2617 με at the buckling load. The hoop strain in the center of dimple, where buckling initiated, was 860 με at buckling. These values are significantly less than the calculated compressive failure strain of −12,280 με and tensile strain of 6584 με (Table 2). Based on maximum strain criterion, it is concluded that the test article failed in buckling rather than due to strength failure.

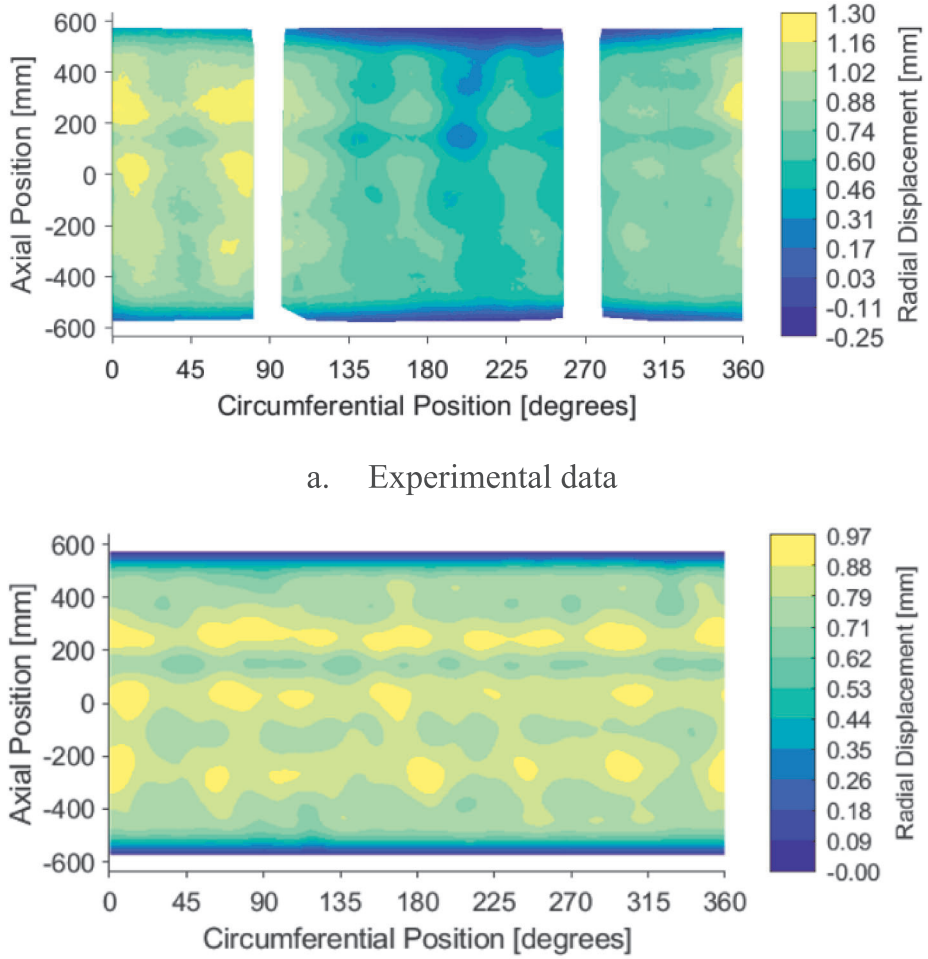

Fig. 19. Radial displacement at 86% of the experimental buckling load.

6.2. Posttest model correlation

While the correlation between the pretest prediction model and the test data was very good, specifically the stiffness and predicted buckling load being within 1%, an additional posttest investigation was completed to determine other variables that may have affected the predicted buckling initiation site. A significant amount of data has been collected on the as-built configuration of NDL-1, such as radial imperfections, thickness variations and shell-end imperfections. There are other possible sources of variation that could not be quantified prior to test. For example, this may include nonuniform loading due to the test frame.

The axial displacements measured just prior to buckling derived from the DIC data at 45, 135, 225, and 315 degrees yielded that the axial displacement at these locations varied from 2.17 mm to 2.21 mm. From these values, a best-fit-plane showed a slight tilt toward the 151-degree circumferential position with an associated maximum axial displacement of 0.021 mm at the shell edge. This corresponds to a rotation of 0.003 degrees of the best fit plane towards the 151-degree circumferential location. To account for this in the FEM, the top reference node was rotated to 0.003 degree from 0 degree linearly over the course of the aforementioned initial prebuckling step, along with the original imposed axial displacement. The rotation was then held constant at 0.003 degree through and after buckling.

The inclusion of the load imperfection changed the buckling load and predicted buckling initiation site. As a result of the tilt, the predicted buckling load was reduced from 2075 kN to 2061 kN. Recall that the experimental load was 2074 kN, which means the adjustment did not improve the prediction of the buckling load with respect to the experimental load. The radial deformations between the models with and without the tilt show a similar global pattern, but the predicted dimple location changed. In the pretest predictions, Fig. 20b, four distinct dimples were centered about the +150 mm axial position starting from 0-degree circumferential position and repeating every 45-degrees with the last dimple at 135-degrees. The prebuckling pattern from the model with the plane tilt is similar, but a single, more prominent dimple formed in the same axial position at 135-degrees, Fig. 25. The predicted buckling initiation site was at the same axial position as the two analyses, but the model still was not able to predict the experimental buckling initiation site centered at 200 degrees.

The load imperfection included in the posttest analysis did not resolve the discrepancy in the radial deformations. One possible explanation for the difference in radial deformation may possibly be attributed to the change in the radial geometric imperfections of the test article from when it was measured after manufacturing, as-manufactured imperfections, to when it was installed in the load frame, as-installed imperfections. It has been shown [23,24] that significant changes in the predicted buckling behavior may be found when

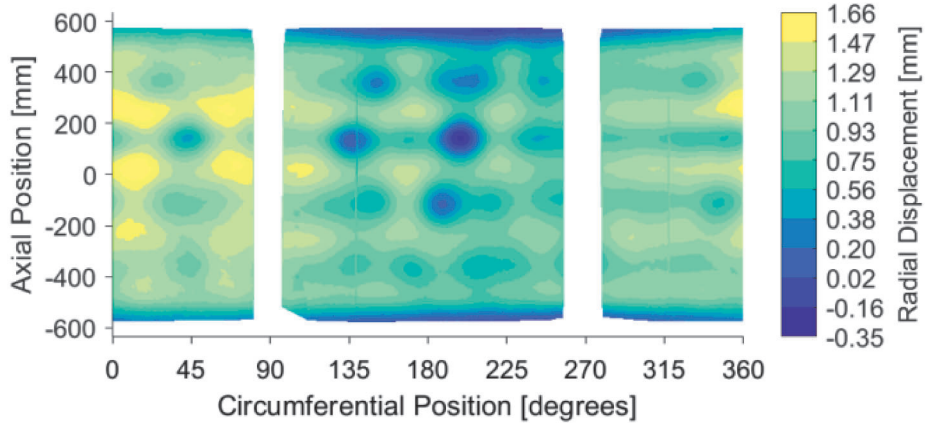

a. Experimental data

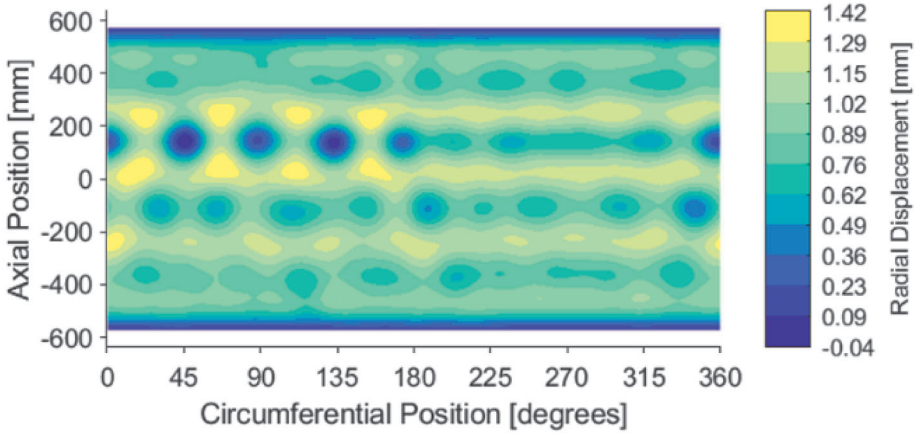

b. FEM data

Fig. 20. Radial displacement immediately prior to the experimental peak load.

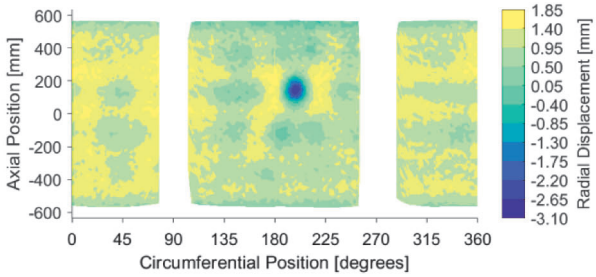

a. First high-speed image

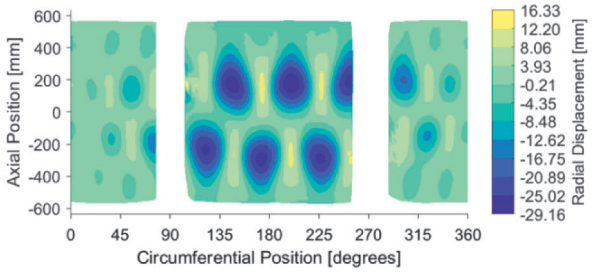

b. Image 5.1 milliseconds after first image

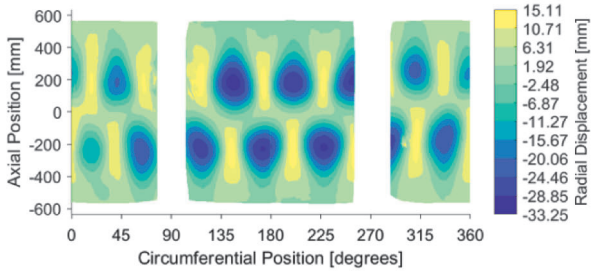

c. Image 7.3 milliseconds after first image

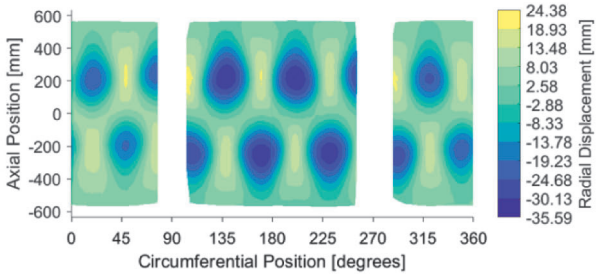

d. Image 16.3 milliseconds after first image

Fig. 21. Buckling propagation measured by high-speed camera.

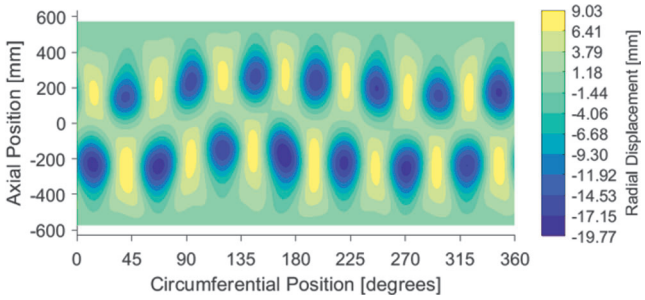

Fig. 22. Predicted postbuckled radial deformation from analysis.

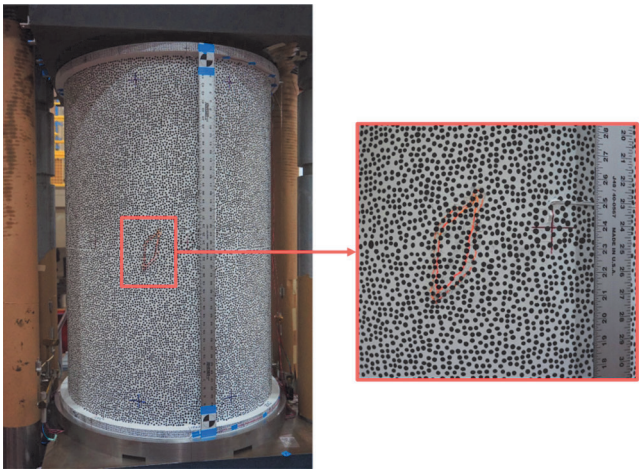

Fig. 23. NDL-1 damage.

the as-installed imperfections were included in the FEMs and compared with the predicted behavior when the as-manufactured (before installation in the test facility) imperfections were included in the FEMs. The full shape of NDL-1 could not be measured in the test frame because the test-frame posts prevented access to sections of the test article.

7. Concluding remarks

Validated finite element models are important for designing buckling-critical launch-vehicle structures, and have been used in the past to perform sensitivity studies and develop new buckling knockdown factor approaches to reduce the mass of launch vehicle components. The objective of this paper was to demonstrate that the scaling methodology was successful at determining a design that would ensure buckling prior to material failure, and to present a modeling methodology to successfully predict the buckling behavior of a scaled, launch-vehicle-like composite cylinder called NDL-1. The finite element modeling approach presented was validated experimentally. The model parameters, the inclusion of as-built details, test and analysis correlation, and a posttest investigation were discussed.

The model parameter study conducted prior to testing was used to determine that the SC8R element performed similarly to the S4R element in analyzing the buckling behavior of a composite cylindrical shell. It was also determined, that while the 10 mm element size was acceptable, a smaller mesh size of 5 mm would better capture NDL1′s imperfection signature measured by structured light scanning, including a prominent feature on the mandrel that transferred to the cylinder during fabrication. The model included features such as measured radial imperfections, thickness imperfections, and shell-end imperfections. In addition, laminate coupon testing was used to develop finite element model lamina properties to best characterize the laminate stiffness.

The results of the finite element model (FEM) correlated well with

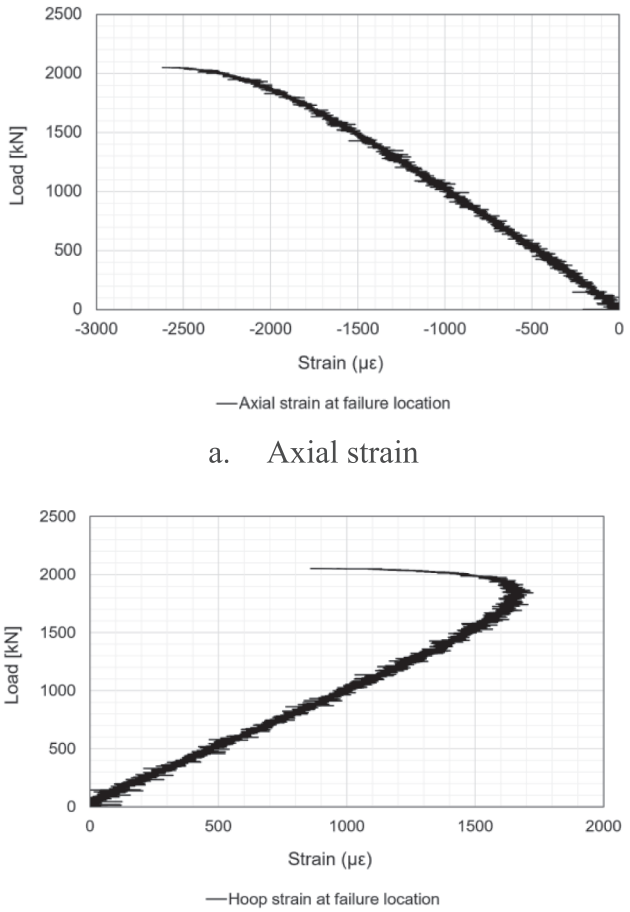

Fig. 24. DIC derived strains in the center of the buckling initiation location.

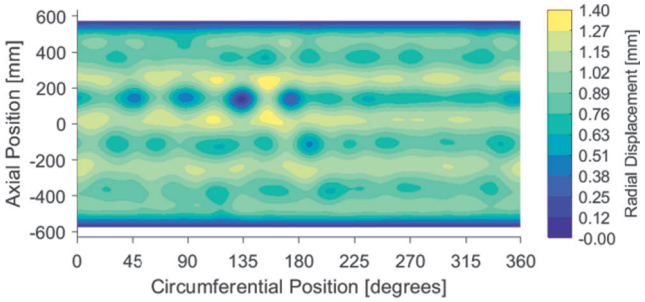

Fig. 25. Radial displacement just prior to buckling with loading imperfection.

the experimental results. The FEM-predicted buckling load was within 0.04% of the experimental buckling load and the predicted stiffness was within 1% of the experimentally measured stiffness. It is speculated that details such as the as-installed imperfection shape could have influenced the shape and magnitudes of the radial deformations. While the magnitudes were quite different, the rate of change of the inward and outward deformation was similar between the finite element model and test. Buckling did initiate in the test at the same axial location as predicted with the FEM, which corresponded to the localized mandrel feature. However, the circumferential location of the buckling initiation site was different between the prediction and test. It was shown with posttest test-analysis correlation that the circumferential buckling initiation site was sensitive to sources of nonuniform loading. The

experimental postbuckling behavior was similar to that of the FEM, but damage that occurred during the buckling event may have influenced the experimental postbuckling behavior. Damage was not considered in the FEA, and this discrepancy was deemed a potential source of deviation in postbuckling observations between test and FEM.

The finite element model presented was shown to produce accurate predictions for the buckling load and stiffness of the scaled, launch-vehicle-like composite shell. The predicted prebuckling, incipient buckling, and postbuckling radial deformations had elements of agreement when compared to the measured radial deformations. Therefore, it is suggested that a similar modeling approach can be employed for other large-scale composite cylindrical shell structures.

CRediT authorship contribution statement

Michelle Tillotson Rudd: Investigation, Writing – original draft, Visualization, Project administration. **David J. Eberlein:** Methodology, Formal analysis, Visualization, Investigation, Writing – original draft. **W. Allen Waters:** Data curation, Writing – review & editing, Supervision. **Nathaniel W. Gardner:** Investigation, Data curation, Writing – review & editing. **Marc R. Schultz:** Conceptualization, Writing – review & editing, Supervision. **Chiara Bisagni:** Conceptualization, Methodology, Writing – review & editing, Supervision.

Declaration of Competing Interest

The authors declare that they have no known competing financial interests or personal relationships that could have appeared to influence the work reported in this paper.

Acknowledgments

The authors would like to thank Ines Uriol Balbin and Kevin van Dooren of Delft University of Technology for the test-article design and analysis support. The work described in this report was conducted as part of the NASA Engineering and Safety Center (NESC) Shell Buckling Knockdown Factor Project, NESC assessment number 07-010-E, in collaboration with the Delft University of Technology.

References

[1] Koiter WT. The stability of elastic equilibrium, NASA AFFDL-TR-70-25; 1970.
[2] Bert CW, Crisman WC, Nordby GM. Buckling of cylindrical and conical sandwich shells with orthotropic facings. AIAA J 1969;7(2):250–7. https://doi.org/10.2514/3.55519.
[3] Card MF. The sensitivity of buckling of axially compressed fiber-reinforced cylindrical shells to small geometric imperfections. NASA 1969:TMX-61914.
[4] Tennyson RC, Muggeridge DB. Buckling of laminated anisotropic imperfect circular cylinders under axial compression. J Spacecraft Rockets 1973;10(2):143–8. https://doi.org/10.2514/3.61860.
[5] Herakovich CT. Theoretical-experimental correlation for buckling of composite cylinders under combined compression and torsion. NASA Contract 1978:NAS1-13175.
[6] Hilburger MW, Starnes Jr JH. High-fidelity nonlinear analysis of compression-loaded composite shells. In the preceedings of the 19th AIAA Applied Aerodynamics Conference, Anaheim, CA, 2001. Paper number AIAA-2001-1394. https://doi.org/10.2514/6.2001-1394.
[7] Khakimova R, Castro SGP, Wilckens D, Rohwer K, Degenhardt R. Buckling of axially compressed CFRP cylinders with and without additional lateral load: Experimental and numerical investigation. Thin-Walled Structures 2017;119:178–89. https://doi.org/10.1016/j.tws.2017.06.002.
[8] Bisagni C. Numerical analysis and experimental correlation of composite shell buckling and post-buckling. Composite Part B: Engingeering 2000;31(8):655–67. https://doi.org/10.1016/S1359-8368(00)00031-7.
[9] Priyadarsini RS, Alyanaraman V, Srinivasan SM. Numerical and experimental study of buckling of advanced fibre composite cylinders under axial compression. Int J Struct Stab Dyn 2012;2(4):1250028. https://doi.org/10.1142/S0219455412500289.
[10] Ghalghachi RN, Showkati H, Firouzsalari SE. Buckling behaviour of GFRP cylindrical shells subjected to axial compression load. Compos Struct 2021;260:113269. https://doi.org/10.1016/j.compstruct.2020.113269.
[11] Hilburger MW. Buckling and failure of compression-loaded composite laminated shells with cutouts. In the preceedings of the 48th AIAA/ASME/ASCE/AHS/ASC Structures, Structural Dynamics, and Materials Conference, Honolulu, HI, 2007, Paper number AIAA 2007-2227. https://doi.org/10.2514/6.2007-2227.
[12] White SC, Weaver PM, Wu KC. Post-buckling analyses of variable-stiffness composite cylinders in axial compression. Compos Struct 2015;123:190–203. https://doi.org/10.1016/j.compstruct.2014.12.013.
[13] Taheri-Behrooz F, Omidi M, Shokrieh MM. Experimental and numerical investigation of buckling behavior of composite cylinders with cutout. Thin-Walled Structures 2017;116:136–44. https://doi.org/10.1016/j.tws.2017.03.009.
[14] Labans E, Bisagni C. Buckling and free vibration study of variable and constant stiffness cylindrical shells. Compos Struct 2019;210:446–57. https://doi.org/10.1016/j.compstruct.2018.11.061.
[15] Labans E, Bisagni C, Celebi M, Tatting B, Gürdal Z, Blom-Schieber A, et al. Bending of composite cylindrical shells with circular cutouts: Experimental validation. AIAA. Journal of Aircraft 2019;56(4):1534–50.
[16] Degenhardt R, Kling A, Bethge A, Orf J, Kärger L, Zimmermann R, et al. Investigations on imperfection sensitivity and deduction of improved knock-down factors for unstiffened CFRP cylindrical shells. Compos Struct 2010;92:1939–46. https://doi.org/10.1016/j.compstruct.2009.12.014.
[17] Hilburger MW. Buckling of thin-walled circular shells. NASA/SP-8007-2020/REV 2; 2020.
[18] Schillo C, Röstermundt D, Krause D. Experimental and numerical study on the influence of imperfections on the buckling load of unstiffened CFRP shells. Compos Struct 2015;131:128–38. https://doi.org/10.1016/j.compstruct.2015.04.032.
[19] Hühne C, Rolfes R, Breitbach E, Teßmer J. Robust design of composite cylindrical shells under axial compression—simulation and validation. Thin-Walled Structures 2008;46(7):947–62. https://doi.org/10.1016/j.tws.2008.01.043.
[20] Wagner HNR, Hühne C, Janssen M. Buckling of cylindrical shells under axial compression with loading imperfections: An experimental and numerical campaign on low knockdown factors. Thin-Walled Structures 2020;151(106764). https://doi.org/10.1016/j.tws.2020.106764.
[21] Schultz MR, Sleight DW, Myers DE, Waters WA, Chunchu PB, Lovejoy AE, Hilburger MW. Buckling design and imperfection sensitivity of sandwich composite launch-vehicle shell structures. In the proceedings of the 31st American Society for Composites Technical Conference, American Society for Composites, Williamsburg, VA; 2016. Paper number AIAA 2018-12029.
[22] Schultz MR, Sleight DW, Gardner NW, Rudd MT, Hilburger MW, Palm T, Oldfield NJ. Test and analysis of a buckling-critical large-scale sandwich composite cylinder. In preceedings of the 59th AIAA/ASCE/AHS/ASC Structures, Structural Dynamics, and Materials Conference, Orland, Florida; 2018. Paper number 1693. https://doi.org/10.2514/6.2018-1693.
[23] Przekop A, Schultz MR, Kosztowny CJR, Gardner NW, Song K, Rudd MT. Buckling test and analysis of the 8-foot-diameter sandwich composite cylinder test article CTA8.2 as part of the Shell Buckling Knockdown Factor Project: Test dates 5-7 December 2017. NASA/TM-20210024095;2022.
[24] Song K, Schultz MR, Kosztowny CJR, Gardner NW, Rudd MT. Buckling test and analysis of the 8-foot-diameter sandwich composite cylinder test article CTA8.3 as part of the Shell Buckling Knockdown Factor Project: Test dates 16-19 December 2019. NASA-TM-20210024768; 2021.
[25] Uriol Balbin I, Bisagni C, Schultz MR, Hilburger MW. Scaling methodology applied to buckling of sandwich composite cylindrical shells. AIAA Journal 2020;58(8):1–10. https://doi.org/10.2514/1.J058999.
[26] Alexander BF, Ng KC. 3D. Shape measurement by active triangulation using an array of coded light stripes. SPIE: Optics, Illumination and Image Sensing for Machine Vision II 1988; 850: 199–209. https://doi.org/10.1117/12.942878.
[27] Hexcel Corporation. HexPly® 8552 Epoxy Matrix (180°C/365°F) curing matrix product data sheet. https://www.hexcel.com/user_area/content_media/raw/HexPly_8552_eu_DataSheet.pdf [accessed May 27, 2020].
[28] Clarkson E. Hexcel 8552 IM7 unidirectional prepreg 190 gsm & 35%RC qualification statistical analysis report. Rev N/C; 2011. Technical Report NCP-RP-2009-028.
[29] ABAQUS/Standard User's Manual. Version 2017 ABAQUS. USA: Inc; 2017.